Composites Science and Technology 225 (2022) 109483

Contents lists available at ScienceDirect

Composites Science and Technology

journal homepage: www.elsevier.com/locate/compscitech

Trade-off between interface stiffening and Young's modulus weakening in graphene/PMMA nanocomposites

Yuanyuan Cui [a,b], Guorui Wang [c], Wenxiang Wang [a,b], Xuwei Cui [a,c], Wenlong Dong [a,b], Congying Wang [a,b], Meihua Jin [a], Tao He [a], Zhong Zhang [c,**], Luqi Liu [a,*]

[a] CAS Key Laboratory of Nanosystem and Hierarchical Fabrication and CAS Center for Excellence in Nanoscience, National Center for Nanoscience and Technology, Beijing, 100190, China

[b] University of Chinese Academy of Sciences, Beijing, 100049, China

[c] CAS Key Laboratory of Mechanical Behavior and Design of Materials, Department of Modern Mechanics, University of Science and Technology of China, Hefei, 230027, China

ARTICLE INFO

Keywords:
Graphene
Nano composites
Interfacial strength
Atomic force microscopy
Raman spectroscopy

ABSTRACT

Mechanical performance of graphene-based polymer nanocomposites is reported to be far below theoretical predictions. A critical factor lies in the weak bonding of graphene/polymer interfaces. Chemical functionalization is deemed as a common strategy to improve the interfacial adhesion between graphene and polymer, however, the creation of structural defects in graphene lattice is inevitable during such a chemical process. It hence calls for a balance in the design of graphene-based nanocomposites between the interface strengthening and mechanical degradation of graphene itself. Herein, mechanically exfoliated monolayer graphene is oxidized and atomic force microscopy (AFM) is performed to quantify the dependence of Young's modulus of graphene on the functionalization degree. In situ tensile-micro Raman spectroscopy is utilized to measure the interfacial properties between functionalized graphene and poly (methyl methacrylate) (PMMA) at the microscopic level. An optimal functionalization degree is determined to maximize the reinforcing effect of nanocomposites. Our results will be helpful to design various nanofiller-based composites with high mechanical performance.

1. Introduction

Graphene possesses high stiffness and strength, large surface area, high aspect ratio, low mass density, and have been envisaged to be the ideal reinforcement for polymer nanocomposites [1–3]. However, numerous published works have shown that the mechanical performance of graphene-based polymer nanocomposites is far below the theoretical predictions [4–6]. A main factor in this regard relates to the inefficient load transfer across graphene/polymer interfaces as dominated by weak van der Waals (vdW) forces [7,8]. To this end, surface modification becomes an effective strategy to improve the interfacial adhesion between graphene and surrounding polymer matrix [9,10]. Among the various chemical and physical treatments [11,12], the chemical oxidation becomes the most widely utilized one not only to improve the dispersion of graphene nanofillers inside polymeric matrix, but also to enhance the interfacial adhesion [13,14]. Meanwhile, the mechanical degradation of graphene nanofillers caused by chemical oxidation has to be taken into account. For instance, compared to pristine graphene, graphene oxide (GO) presented relatively lower Young's modulus and breaking strength owing to the presence of structural defects [15–18]. Recent molecular dynamics (MD) simulations revealed that by tuning the extent and chemistry of the functionalized species reaching ~10–20%, the graphene-based PMMA nanocomposites could achieve an increase of 46% in Young's modulus and 119% in energy absorption during facture [19]. Employing the similar method, Singh et al. reported that ~10% carboxyl functionalized graphene-based composites resulted in 44% increase in the Young's modulus at the interfacial region compared to pristine graphene-based composites [20]. Despite these progresses, from the experimental points of view, there is still lack of direct evidence to confirm the relationship between the optimized functionalized degrees and maximum reinforcing capability of graphene nanofillers.

With the help of In situ tensile-micro Raman spectroscopy, monolayer graphene with micrometer lateral size makes it of promise for

* Corresponding author.
** Corresponding author.
E-mail addresses: zhongzhang@ustc.edu.cn (Z. Zhang), liulq@nanoctr.cn (L. Liu).

https://doi.org/10.1016/j.compscitech.2022.109483
Received 21 February 2022; Received in revised form 21 April 2022; Accepted 24 April 2022
Available online 5 May 2022

monitoring the in-plane strain, and hence the detection of interfacial behaviors at the microscopic level [21–28]. For instance, Gong et al. have monitored the stress transfer in monolayer graphene sandwiched between the PMMA and the SU-8 polymer layer. The derived interfacial shear strength was on the order of 0.3–0.8 MPa [22]. Similar results were also reported for monolayer graphene-based polyethylene terephthalate (PET) nanocomposites [23]. Later, our group systematically investigated the impact of chemical bonding types on the interfacial properties and failure modes of graphene/PMMA interface at the microscopic level [25]. Owing to the formation of hydrogen bonds (H bonds) between oxidized graphene and the PMMA substrate, the interfacial shear stress transfer efficiency was improved greatly. Nevertheless, it should be noted that the influence of degraded Young's modulus of graphene fillers on the interfacial shear strength has not been considered yet in previous work. A balance between the improvement in interfacial load transfer efficiency and the degradation in Young's modulus of graphene nanofillers still needs exploration.

Herein, various oxygen-containing groups (e.g., hydroxyl groups, carboxylic groups, and epoxide groups) were introduced to the monolayer graphene surface via UV-Ozone treatment. Similar to our previous work [25], H bonds are expected to form between oxidized graphene and PMMA substrate. Atomic force microscopy (AFM) nanoindentation tests were conducted to quantify the dependence of Young's modulus of monolayer graphene on the functionalized degrees. Meanwhile, in situ tensile micro-Raman spectroscopy was used to monitor the interfacial shear stress transfer at the microscopic level, and further quantitively evaluate the impact of functionalized degrees of graphene on the interfacial shear strength. Our results revealed that the optimization of functionalized degrees of graphene nanofiller is important to maximize the reinforcing effect of nanocomposites.

2. Experimental section

2.1. Sample preparation

The graphene samples were prepared by mechanical cleavage and adhered to Si wafer with a 300 nm SiO_2 capping layer. Optical microscopy was used to locate the graphene sheet and determine the layer of graphene preliminarily, and further confirmed by micro-Raman spectroscopy. A thin layer PMMA ($M_w \approx 30{,}000$ g/mol, 4 wt% in acetone) was spin-coated on the silicon substrate at the speed of 3000 r/min, and heated for 3 min at 75 °C and then for 5 min at 120 °C. The resulting thickness of PMMA layer was nearly 300 nm as characterized by atomic force microscope (AFM) Afterward, 1 M NaOH aqueous solution was used to detach the PMMA/graphene layer from the silicon wafer by etching the surface of SiO_2, which was then cleaned with deionized water. Finally, a thin PMMA membrane with graphene sheets attached was obtained. The monolayer graphene sheet was then successfully transferred onto the surface of the PMMA film as the substrate. Fig. 1a shows the whole experiment flow chart. The characteristic Raman peaks as shown in Fig. 1b indicate the success of the transfer process. Meanwhile, the identical lateral size and shape of graphene sheets are observed in two substrates as shown in the inset of Fig. 1b.

2.2. Oxidation and characterization of monolayer graphene sheets

Oxidization of individual graphene sheet was performed by UV-ozone (UVO) treatments (Jelight UV-Ozone cleaner model-24). Exfoliated graphene sheets deposited onto Si substrate were placed into the chamber, in which the distance between the UV-source and the substrate were kept 20 mm. The reaction time was varied from 2 to 8 minutes in order to control the functionalization degrees of monolayer graphene sheets. Renishaw Raman spectrometer was used to identify the layer number of graphene and functionalization degrees (denoted by I_D/I_G). The laser wavelength was 514 nm and the laser power was kept below 1.0 mW to avoid laser induced local heating of the sample. The focused laser spot was approximately 1 μm in diameter. Graphene sample was placed on calcium fluoride substrate and Microscopic Fourier transform infrared spectrometer (FTIR) (transmission mode, Thermo Fisher, Nicolet iN10) was used to identify various oxygen-containing groups attached on the graphene sheet.

2.3. In situ tensile-micro Raman test

The mechanical deformation of graphene sheet was carried out with a PMMA substrate (length: 30 mm, width: 5 mm, thickness: 0.2 mm) clamped by a home-made tensile stage. The tensile strain was applied with an increment step of ~0.05% to ~0.1%. All Raman bands of graphene were fitted with Lorentzian functions. To obtain the strain distribution on the graphene sheet, the tested monolayer graphene sheets were moved with a step size of 300–500 nm depending on the graphene lateral size. Meanwhile, Raman spectra were recorded with an interval of 300 or 500 nm within the sheets.

2.4. AFM nanoindentation test

An array of circular holes was patterned onto silicon substrates covered with a 300 nm thick SiO_2 layer through photolithography and reactive ion etching. The depth is ~1 μm and the diameter ranges from 3 to 5 μm. Monolayer graphene was directly adhered to the pre-patterned substrates to cover the circular holes. A commercial AFM system (Asylum Research, MFP-3D Infinity) was used to perform the

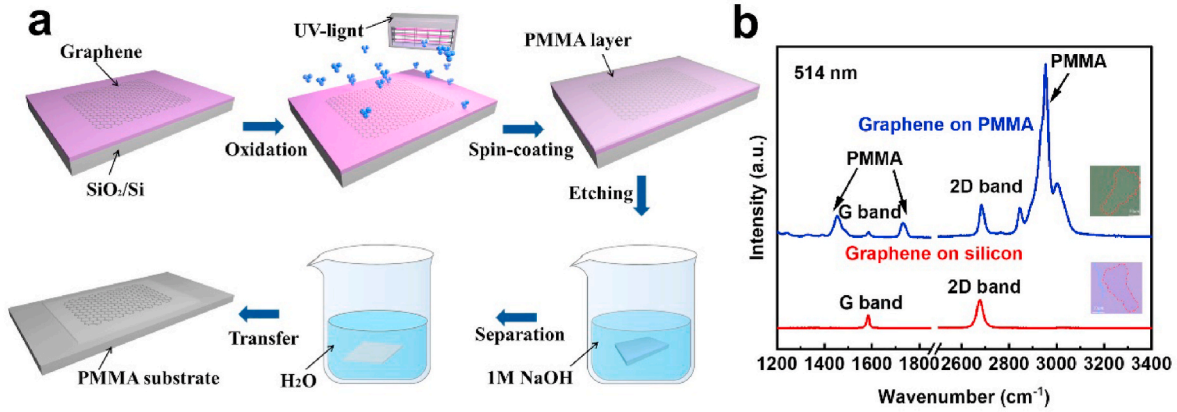

Fig. 1. (a) Schematic illustration of the sample preparation process. (b) Raman spectra of pristine graphene sheet deposited onto silicon and PMMA substrates. The insets are the optical images of the graphene sheet before and after transfer with the help of PMMA supporting layer. (For interpretation of the references to color in this figure legend, the reader is referred to the Web version of this article.)

nanoindentation test on the suspended part of graphene. The AFM tip (Nanotec Instruments, radius: 60 nm) was centered in the geometric center of the circular hole. The cantilever spring constant (ranging from 30 to 40 N/m) was calibrated by Sader method [29] before every series of testing. Young's modulus of the tested samples was determined through the fitting force curves which were obtained from the AFM nanoindentation test as the force increased. All the measurements were conducted at the same loading/unloading rate (300 nm/s).

3. Results and discussion

3.1. Chemical functionalization of monolayer graphene sheet

A tabletop UVO with a low-pressure mercury UV-light generating UV-emissions at 185 nm and 254 nm wavelengths, respectively, was used to induce oxygen-containing groups on the graphene sheets (see Experimental section). In principle, the 185 nm wavelength could be absorbed by oxygen, and accounted for the generation of ozone. Comparatively, the 254 nm radiation was only absorbed by ozone instead of oxygen, principally responsible for the destruction of ozone in the UV box. Therefore, in the case of both wavelengths available, ozone is continually formed and destroyed. An intermediate product of both the formation and destruction processes is atomic oxygen, which is a strong oxidizing agent [30]. Fig. 2a shows the typical micro-FTIR spectra of the monolayer graphene sheets treated by UVO at different times. The various oxygen-containing groups such as hydroxyl, carboxyl, and epoxy groups are successfully attached onto the surface of the graphene sheets. As expected, the stretching mode of ν(C═C) at 1580 cm^{-1} in the graphene backbone are observed for pristine graphene sheet. After oxidation treatment, new peaks emerge at 1730 cm^{-1} and 1250 cm^{-1} related to stretching mode of ν(C═O) and ν(C-O-C) respectively, and the band around 1400 cm^{-1} is assigned to the in-plane bending vibration of hydroxyl groups [31]. The relative intensity ratio of oxygen-containing groups with respect to C═C band apparently increases upon prolonging the oxidation treatment times. After the ozone treatment, the oxidized monolayer graphene sheet was then transferred from silicon substrate to a flexible PMMA substrate as depicted in Fig. 1a. Expectedly, the H bonds will form between hydroxyl, carboxylic groups in oxidized graphene and ester groups in PMMA as depicted in Fig. 2b.

Meanwhile, Raman spectroscopy was used to characterize monolayer graphene and oxidized graphene sheets. Fig. 2c shows the evolution of the Raman spectra of graphene and oxidized graphene with different reaction times. For pristine monolayer graphene, there are only G and 2D band at 1580 cm^{-1} and 2680 cm^{-1} respectively. Interestingly, there was no significant D band observed due to the insufficient ozone concentration in the reaction chamber within a short reaction time (1–2 min). When the reaction lasts for 3 min, the apparent Raman D band at ~1350 cm^{-1} and D′ band near the G band at 1580 cm^{-1} are observed for the oxidized graphene sheets, indicating the conversion of sp^2 carbon to sp^3 carbon due to the oxygen-containing groups grafted onto the graphene sheet. With the prolonged reaction time above 5 min, Raman D + D′ band appears at 2940 cm^{-1}. Typically, the intensity ratio of Raman D band and G band (I_D/I_G) has been involved to quantify the functionalization degrees of graphene sheet [32,33]. As depicted in Fig. 2d, the increased trend of the Raman intensity ratio of I_D/I_G as a function of reaction times was observed at earlier range (≤7 min), implying the increase in the functionalization degrees of the oxidized monolayer graphene sheets (e.g., $I_D/I_G = 0.13 \pm 0.09$ for 3 min, $I_D/I_G = 2.92 \pm 0.25$ for 7 min). After 7 min treatment, the I_D/I_G shows an apparently decreased trend along with the broadening of FWHM (full width at half maximum) of Raman D band from 33 cm^{-1} to 57 cm^{-1}, which might relate to the generation of vacancy defects owing to the coalescence of point defects induced structural disorder of six-atom carbon rings [34]. It is worth noting that the Young's modulus would significantly decrease once the functionalization degrees of graphene is relatively high. Thus, in the subsequent nanoindentation tests, we mainly concentrated on the

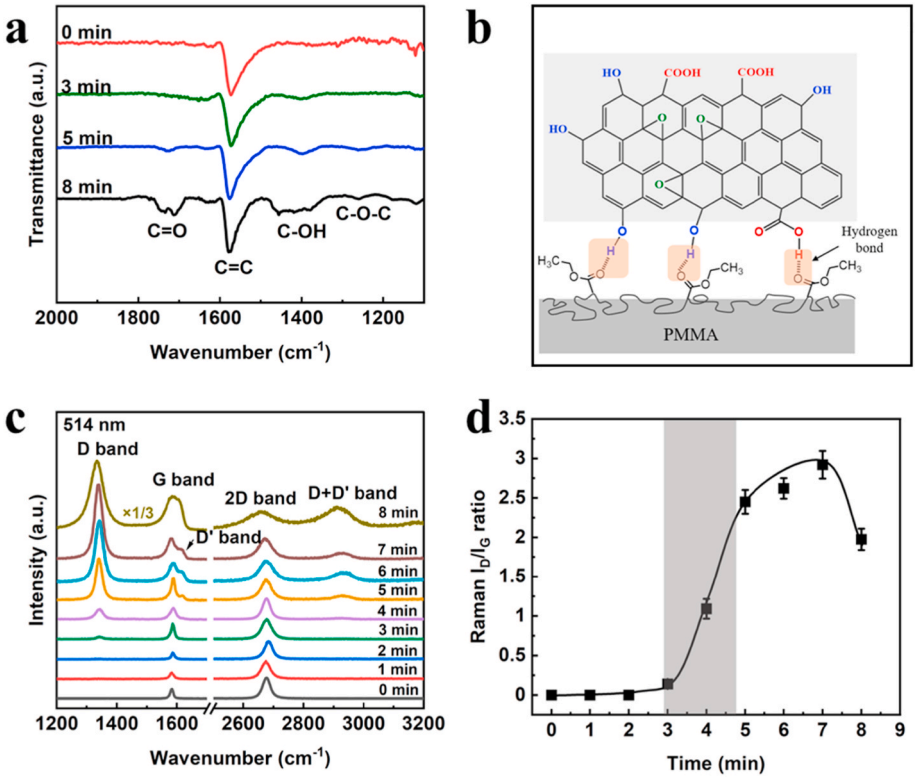

Fig. 2. (a) Micro-FTIR spectra of monolayer graphene sheet treated at different oxidation times. (b) The schematic diagram of the formation of H bonds between oxidized graphene and PMMA matrix. (c) Raman spectra of oxidized graphene sheets treated at different reaction times. (d) The evolution of Raman I_D/I_G as a function of reaction times. The black solid line is guide to eyes and gray shaded region is the interest in this work.

sp^3-type graphene sheets.

3.2. Monitoring the load transfer of graphene and oxidized graphene/PMMA interface by in situ tensile micro-Raman spectroscopy

Raman spectroscopy has been successfully employed to detect the deformation of graphene sheets at the microscale [35–37]. Given the fact that Raman 2D peak shift rate is approximately twice higher than Raman G peak in tension [38], herein, we monitor the strain in graphene sheet based on the shifted trend of Raman 2D band as presented in Fig. 3a. Fig. S3a presents the relationship between Raman 2D peak position and the applied strain, indicating -46 cm^{-1}/% Raman 2D band shift rate for monolayer graphene/PMMA model system, which is consistent well with the values reported previously for a graphene/PMMA laminate (-51 cm^{-1}/%) and a graphene/PET laminate (-52.5 cm^{-1}/%) [23,25,39]. Meanwhile, owing to formation of hydrogen bonding between functionalized graphene and PMMA, the Raman 2D peak shift rate shows apparently decreased trend with increasing functionalized degrees. Detailed information is summarized in Fig. S3.

To describe the interfacial stress transfer process in the monolayer graphene polymer nanocomposite, the conventional shear lag model was utilized in earlier works [22,23,40]. Assuming that the graphene/PMMA interface was elastic at low strain level (e.g., $\varepsilon_m \leq 0.2\%$), the strain distribution in the graphene sheet (ε_g) as a function of the position (x) along the length direction could be predicted by the following Equation (1):

$$\varepsilon_g = \varepsilon_m\left(1 - \frac{\cosh(\beta x)}{\cosh(\beta L/2)}\right) \tag{1}$$

where ε_m is the applied strain of PMMA matrix, L is the length of graphene along the deformation direction, $\beta = \sqrt{k_m/E_g t}$ is the shear-lag parameter which is typically treated as an effective measure for the efficiency of interfacial stress transfer. The value of β depends on the effective stiffness of the substrate (k_m) and the in-plane stiffness of monolayer graphene (E_g) [6,23]. Based on Equation (1), it is indicated that the maximum strain of graphene occurred at the center ($x = 0$) and maximum interfacial shear stress occurred at the edges ($x = \pm L/2$). According to our experimental results shown in Fig. 3c, the strain distribution of the graphene sheet can be fitted well by Equation (1) at the relatively low strain level (e.g., $\varepsilon = 0.16\%$) (red curves in Fig. 3c and d). Beyond the critical applied strain (ε_c), graphene starts sliding from edges and the sliding zones at two ends gradually approach the center of the sheet, where s represents the length of sliding zone. Consequently, Equation (1) no longer predicts the strain. However, Equation (1) is still applicable to the non-sliding zone, the boundary condition requires the axial force in graphene to be continuous at ($x = \pm L/2 - s$) [41]. Therefore, the strain distributions in graphene are calculated by the non-linear shear-lag analysis via the following Equation (2) [22,23,42]:

$$\varepsilon_g = \varepsilon_m - \frac{\tau_c}{\beta E_g t}\frac{\cosh(\beta x)}{\sinh(\beta(L/2 - s))} \tag{2}$$

In the sliding zone, based on the linear slope of the triangle-like strain distribution feature, the interfacial shear strength τ_c can be derived by the following Equation (3):

$$\tau_c = E_g t\frac{d\varepsilon}{dx} \approx E_g t\frac{\varepsilon_p}{L/2} \tag{3}$$

where E_g is the Young's modulus of graphene sheet, t is the thickness of graphene, $\frac{d\varepsilon}{dx}$ is the slope of strain gradient in sliding zones, and ε_p is plateau strain. Fig. 3c shows the strain distribution of pristine monolayer graphene sheet along the tensile direction at different applied strain levels. Thus, the derived shear strength for vdW dominated monolayer graphene/PMMA interface is 0.25 ± 0.03 MPa by taking $E_g = 964 \pm 81$ GPa, $t = 0.34$ nm, $\frac{d\varepsilon}{dx} = 0.077 \pm 0.004$ %/μm, which is consistent with the previously reported values [25].

To further reveal the effect of H bonds on the interfacial shear strength as well as its dependence on the functionalization degrees of the

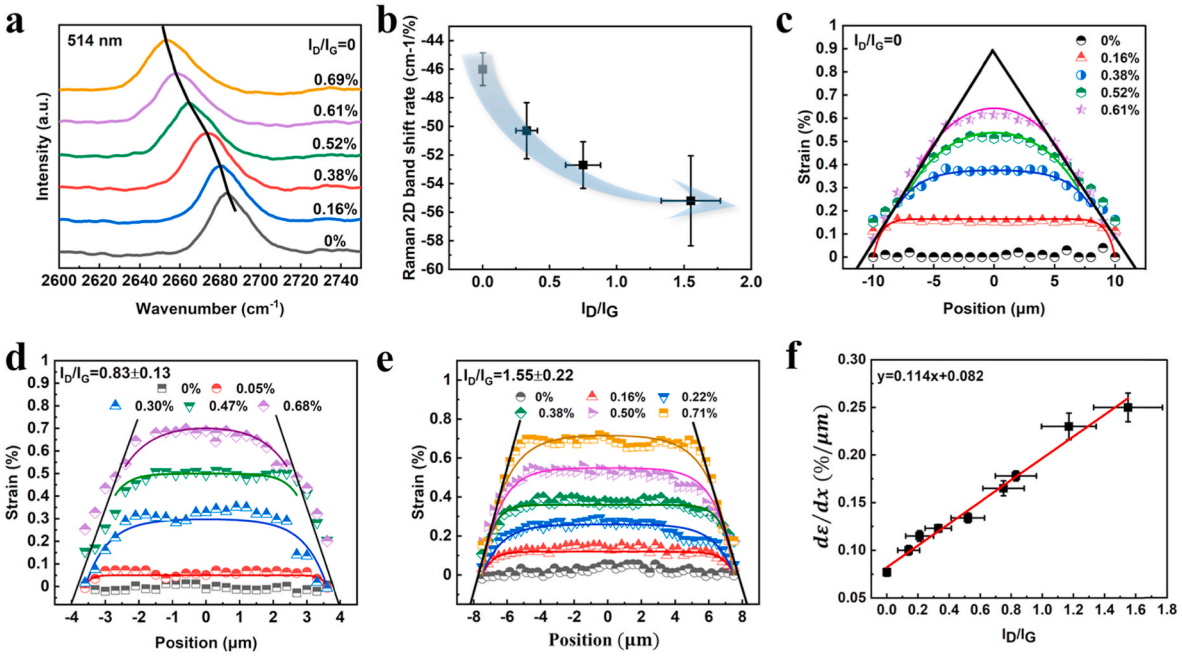

Fig. 3. (a) Evolution of Raman 2D spectrum of monolayer graphene sheet with increasing applied strain. The black solid line is guide to eyes. (b) The relation between I_D/I_G and Raman 2D band shift rate. All the data can be found at Figure S3 (c-e) Strain distribution in the direction of the tensile axis of the (c) pristine graphene sheet and oxidized graphene sheet (d, e) at different strain levels. The Raman data points in sliding zone are fitted by the black solid lines based on the nonlinear shear-lag model to extract $\frac{d\varepsilon}{dx}$. The colored solid lines (blue, green and purple) represent the fitted curves by Eq. (2). (f) The strain gradient as a function of the Raman intensity ratio of I_D/I_G in graphene/PMMA composites. Data points are summarized in Table S1. The red solid line is a linear fitting curve. (For interpretation of the references to color in this figure legend, the reader is referred to the Web version of this article.)

oxidized graphene sheet, herein, the monolayer graphene sheets with varied functionalization degrees are investigated. Fig. S1 shows the typical Raman mapping image of the oxidized graphene sheet with $I_D/I_G = 1.55 \pm 0.22$. The uniformly distributed I_D/I_G values within the whole sheet implied the successful introduction of oxygen-containing groups onto graphene surface. Fig. 3d and e shows the strain distribution of oxidized graphene sheet ($I_D/I_G = 0.83 \pm 0.13$, $I_D/I_G = 1.55 \pm 0.22$) along the tensile direction at different applied strain levels. It can be seen from the fitting results that the corresponding slopes $\frac{d\varepsilon}{dx}$ for H bonds dominated interface are higher than those of vdW dominated interface. Fig. 3f shows the trend of the $\frac{d\varepsilon}{dx}$ values as a function of I_D/I_G of the oxidized graphene sheet. The $\frac{d\varepsilon}{dx}$ tends to increase from 0.077%/μm to 0.230%/μm, and the corresponding β value tends to increase from 0.5 μm^{-1} to 1.6 μm^{-1} linearly with the increasing I_D/I_G of up to ~1.55, indicating that the H bonds at the interface enhances the interfacial shear transfer efficiency unambiguously. Furthermore, the specific $\frac{d\varepsilon}{dx}$ value with respect to a given I_D/I_G can be estimated roughly through the fitting formula in Fig. 3e. Comparatively, the derived $\frac{d\varepsilon}{dx}$ values are aligned with the previous results for PMMA/graphene/SU-8 laminate ($\frac{d\varepsilon}{dx}$ = 0.088–0.240%/μm) [22] and oxidized graphene/PMMA laminate ($\frac{d\varepsilon}{dx}$ = 0.14–0.50%/μm) [25].

3.3. Measurement of Young's modulus of oxidized monolayer graphene

Suspended monolayer graphene sheets were directly exfoliated on pre-patterned silicon substrates as shown in Fig. 4a. To oxidize monolayer graphene sheet, each sample was exposed to UVO for a given time followed by micro-Raman characterization. Likewise, the Raman parameter of I_D/I_G ratio was used to quantify the degrees of functionalization of the oxidized graphene sheets. Detailed information is presented in Fig. S2. Fig. 4b shows typical force-displacement curves for pristine monolayer graphene and oxidized monolayer graphene. It is obvious that the maximum breaking force of functionalized graphene decreases significantly, reflecting the reduction of graphene breaking strength, which is in accord with the previous data [15]. The relationship between breaking strength and I_D/I_G ratio as presented in Fig. S7. In order to obtain Young's modulus of functionalized graphene, the indentation process was modeled as clamped circular membranes with a central point loading, which offered Equation (4) consisting of a linear and cubic deflection term to determine in-plane elastic modulus:

$$F(\delta) = \pi\sigma_0\delta + E_g t\delta^3/a^2 \quad (4)$$

where F is the loading force, δ is the indentation displacement at the central point, a is the radius of patterned holes, t is thickness of graphene (0.34 nm here) [43], σ_0 is the pretension accumulated in the sheets. However, a number of recent advances have pointed out the possibly error of this equation [44,45], present data were analyzed in Fig. S5 to check how the experimental results deviate from this equation. For pristine monolayer graphene, the extracted Young's modulus ranges from 800 to 1100 GPa, with an average of 964 ± 81 GPa in good agreement with previous reports [1,15,46]. Apparently, Young's modulus decreases significantly with increasing I_D/I_G for oxidized monolayer graphene sheets, even reaching ~50% of the pristine sheet at I_D/I_G ≈0.91. It should be noted that the suspend graphene sheets will fail once the I_D/I_G ratio was relatively high, hence, the nanoindentation tests were concentrated on the samples with $I_D/I_G < 1$. Fig. 4c shows the evolution of the Young's modulus as a function of the Raman I_D/I_G ratios. The decreased trend of Young's modulus with increasing functionalized degrees was in accordance with the earlier reports for plasma treated graphene sheets [9]. Fig. S6 presents the relationship between Young's modulus and I_D/I_G ratio. All the data can be found at Table S2.

3.4. Optimization of reinforcing effect of graphene-based nanocomposites

As stated earlier in Equation (3), the value of τ_c is affected by $\frac{d\varepsilon}{dx}$ and E_g. In our earlier work [25], the value of E_g was considered as the constant for the oxidized graphene sheets, so the τ_c tends to increase linearly and then reaches a plateau region with the increasing Raman intensity ratio of I_D/I_G. However, when we consider the effect of Young's modulus of oxidized graphene sheets on the interfacial shear strength,

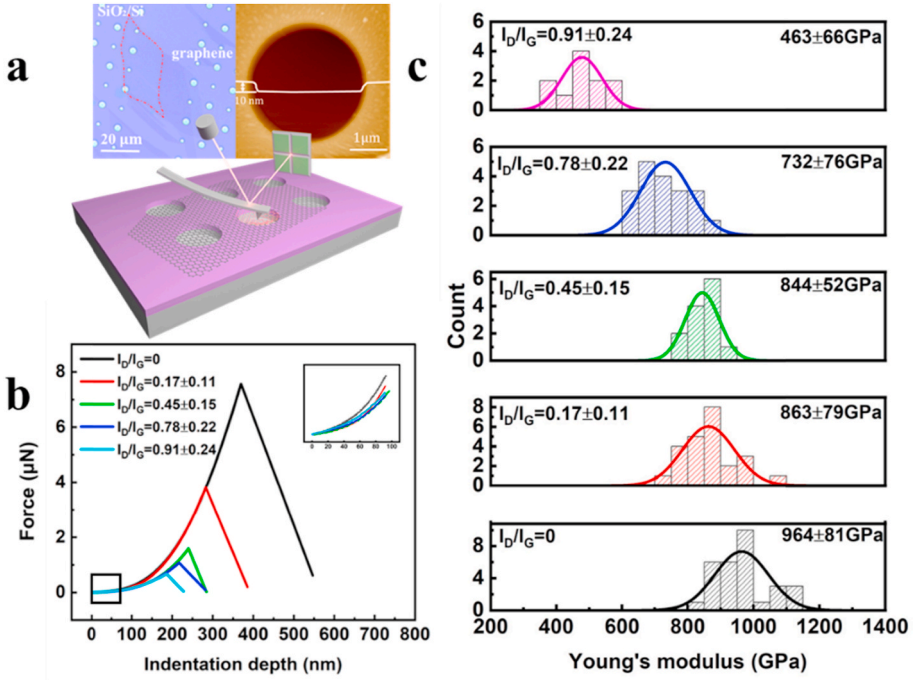

Fig. 4. (a) Schematic representation of AFM nanoindentation test on suspended monolayer graphene sample. The insets are is optical image and AFM image of suspended monolayer graphene. (b) Typical force curves for pristine and oxidized monolayer graphene samples (Insets are curves in the black box). (c) Histogram of Young's modulus for pristine and oxidized monolayer graphene samples. Solid lines represent Gaussian fits to the data.

the conclusion will be different. Based on our experimental design, the relationship between $\frac{d\varepsilon}{dx}$, E_g and I_D/I_G can be easily revealed. From an experimental viewpoint, however, it is hard to have the exact same I_D/I_G ratios for the samples utilized both for nanoindentation and in situ tensile-Raman tests owing to the substrate effect [47]. Herein, for a given I_D/I_G ratio, the value of E_g was derived directly from nanoindentation tests while the value of $\frac{d\varepsilon}{dx}$ is given through the fitting formula as shown in Fig. 3e. Fig. 5a shows the trend of the interfacial shear strength as a function of the Raman intensity ratio ($I_D/\ I_G$) of the oxidized graphene sheets. The τ_c tends to increase from 0.2 to 0.4 MPa and reaches a maximum value with the increasing Raman intensity ratio of I_D/I_G from 0 to 0.8, indicating the H bonds at the interface enhance the interfacial interaction. With a further increasing Raman intensity ratio of I_D/I_G, the τ_c tends to decrease significantly, implying that the weakening of Young's modulus plays a dominant role in Equation (3). Based on our experimental results, we demonstrated that the enhanced load transfer for oxidized graphene/PMMA system with functionalization degrees located in the range of 0.6–0.8. The values in Fig. 5a can be found in Table S3.

As well known that the mechanical reinforcement of nanocomposite is critically dependent on the quality of interfacial interaction and the load bearing capability of nanofillers [48]. The high interfacial strength and large aspect ratio favor efficient load transfer from matrix to filler, and then the filler could carry more loads to reinforce the composites [6]. As stated earlier, however, the introduction of oxygen-containing groups would create defects in the graphene lattice, and then compromise the intrinsic mechanical property of graphene. Therefore, the weakening in Young's modulus of graphene sheets and its impact on the reinforcement in nanocomposites has to be considered. To quantitatively evaluate the impact of various parameters on the loading bearing capability of graphene sheets in nanocomposites (e.g., orientation, agglomeration, interfacial interaction, and defects), the effective modulus (E_{eff}) of graphene nanofillers is expressed by the following Equation (5):

$$E_{eff} = \eta_o \eta_a \eta_L E_g = E_g \left[1 - \frac{\tanh\left(\frac{\beta L}{2}\right)}{\frac{\beta L}{2}} \right] \tag{5}$$

where η_o is the orientation factor, η_a is the agglomeration factor, η_L is the length factor which represents the stress bearing efficiency of different sizes of graphene in the polymer matrix, and E_g is the modulus of oxidized graphene and dimensionless group βL is the fitting parameter as mentioned above (Table S1). In our model composite system, there is no question of orientation and agglomeration, so we have $\eta_o = 1$ and $\eta_a = 1$. The dependence of β and E_g on the I_D/I_G ratio can be clarified by the fitted results as presented in Fig. S4 and S6. Fig. 5b shows the bearing efficiency of model graphene composites as a function of sheet size. The solid lines are drawn by the formula $\eta_L = \left[1 - \frac{\tanh(\beta L/2)}{\beta L/2}\right]$. Obviously, for the graphene sheet with smaller size, it cannot effectively bear stress even if β is large (e.g., $\beta = 2$, $L = 3$ μm, $\eta_L = 0.67$). In contrast, the graphene sheet with sufficient lateral size exhibits a higher load-carrying capability regardless of β (e.g., $\beta = 0.5$, $L = 40$ μm, $\eta_L = 0.9$). Consistently, the experimental data with β ranged from 0.34 to 1.36 are scattered within those theoretical curves. For instance, for the graphene sheet with a given length (e.g., ~15 μm), the increased trend of β values would favor the efficient load-bearing capability. Together with the experimental results, Fig. 5c summarizes the effective modulus of graphene filler as a function of I_D/I_G ratios. The solid line and the points represent the theoretical prediction and experimental results respectively, and the color bar corresponds to a change in the length of the graphene sheet. It is clear that, in a proper range of I_D/I_G ratio and similar sample size, the chemical functionalization, though decreasing the Young's modulus of graphene, could improve the effective modulus through the stiffening effects on the interfacial stress transfer efficiency. However, with further increase in the functionalized degrees, the reinforcing role reaches the saturation and cannot counteract the structural defects induced mechanical degradation, finally leading to counterproductive results. Interestingly, for the pristine graphene, due to the large sample size (the red point), the calculated value of effective modulus is

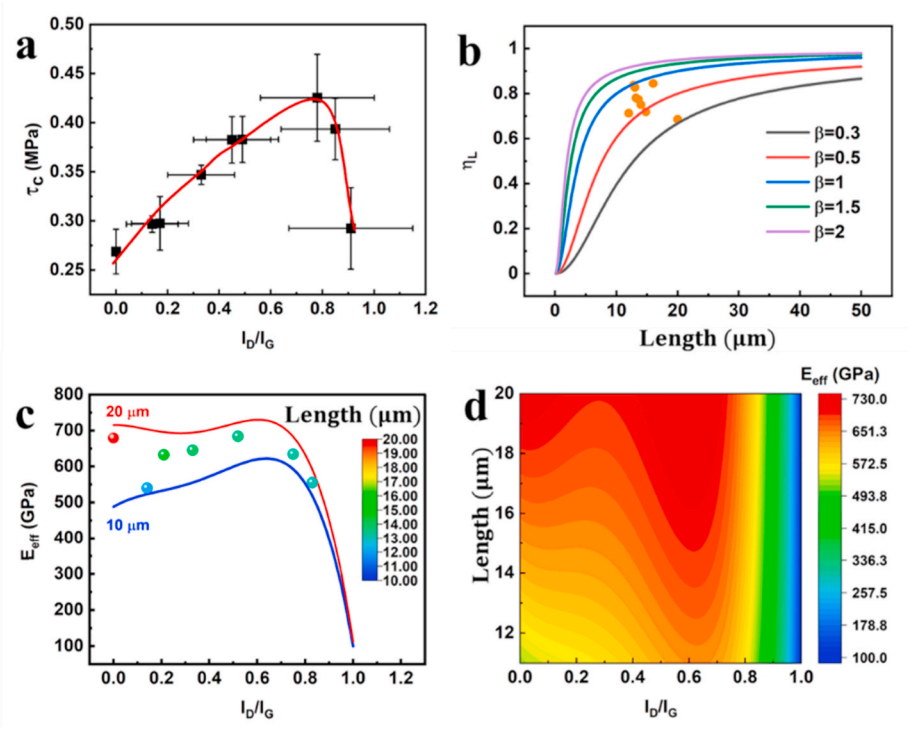

Fig. 5. (a)The interfacial shear strength (τ_c) as a function of the Raman intensity ratio I_D/I_G in graphene/PMMA nanocomposite system. The solid red line is guided for eyes. (b) The length factor η_L as a function of the length of graphene with various β values. (c) The effective modulus of oxidized graphene in the nanocomposite as a function of the intensity ratio (I_D/I_G), corresponding with various β values. (d) Theoretical prediction of effective modulus of graphene of different intensity ratio I_D/I_G and lengths. (For interpretation of the references to color in this figure legend, the reader is referred to the Web version of this article.)

larger than that of oxidized graphene, which further proves that a large aspect ratio is conducive to effective load transfer. Thus, the optimal functionalized degrees and sample size should be considered in efforts to design graphene-based nanocomposites with high mechanical performance. Based on the experimental results and formula fitting, Fig. 5d further shows the synergistic effect of the functionalized degrees and sample length on the effective Young's modulus in composites. Analogous to conventional composites [49,50], large aspect ratio of graphene sheet, from the perspective of interface, would benefit the efficient load transfer and the effective modulus. Especially, considerably large graphene flakes, with less functionalization and hence defects, could fully realize the mechanical properties of graphene.

4. Conclusion

The effect of the oxidation of graphene nanofillers on the interfacial shear strength was examined for the monolayer graphene/PMMA nanocomposite system by means of in situ tensile micro-Raman and AFM nanoindentation technique. Due to the formation of H bonds between graphene and PMMA matrix, the interface was stiffening with increasing functionalization degrees. Meanwhile, the chemical oxidation degraded elastic modulus and strength of graphene sheets significantly. Therefore, there is a balance to be struck in the design of graphene-based nanocomposites between the ability to achieve efficient load transfer and the reduction in the elastic modulus of the oxidized graphene. The optimal functionalization degree ($I_D/I_G = 0.78 \pm 0.22$) is proposed to achieve the maximum effective modulus for the nanocomposite. Our work on the interfacial mechanics between graphene and PMMA offer valuable insight and a design guideline for the enhanced functionalization of graphene with proper surface chemical groups as well as implementing reinforcing effects.

CRediT authorship contribution statement

Yuanyuan Cui: Experiment, Methodology, Data curation, Formal analysis, Writing – original draft. **Guorui Wang:** Methodology, Investigation, Data curation, Formal analysis, Validation, Writing – original draft. **Wenxiang Wang:** Experiment, Writing – review & editing. **Xuwei Cui:** Formal analysis, Validation, Theoretical analysis and validation. **Wenlong Dong:** Writing – original draft. **Congying Wang:** Writing – original draft. **Meihua Jin:** Experiment. **Tao He:** Experiment. **Zhong Zhang:** Supervision, Project administration, Funding acquisition, Resources. **Luqi Liu:** Supervision, Project administration, Funding acquisition, Resources, Writing – review & editing.

Declaration of competing interest

The authors declare that they have no known competing financial interests or personal relationships that could have appeared to influence the work reported in this paper.

Acknowledgments

This work is jointly supported by the National Natural Science Foundation of China (Grant Nos. 22072031, 11832010, 11890682), the Strategic Priority Research Program of Chinese Academy of Sciences (CAS) under the Grant Nos XDB30020100.

Appendix A. Supplementary data

Supplementary data to this article can be found online at https://doi.org/10.1016/j.compscitech.2022.109483.

References

[1] C. Lee, X. Wei, J.W. Kysar, J. Hone, Measurement of the elastic properties and intrinsic strength of monolayer graphene, Science 321 (2008) 385–388, https://doi.org/10.1126/science.1157996.
[2] Y. Zhu, S. Murali, W. Cai, X. Li, J.W. Suk, J.R. Potts, R.S. Ruoff, Graphene and graphene oxide: synthesis, properties, and applications, Adv. Mater. 22 (2010) 3906–3924, https://doi.org/10.1002/adma.201001068.
[3] I.A. Kinloch, J. Suhr, J. Lou, R.J. Young, P.M. Ajayan, Composites with carbon nanotubes and graphene: an outlook, Science 362 (2018) 547–553, https://doi.org/10.1126/science.aat7439.
[4] P. Kannan, R.J. Young, S.J. Eichhorn, Debundling, isolation, and identification of carbon nanotubes in electrospun nanofibers, Small 4 (2008) 930–933, https://doi.org/10.1002/smll.200800136.
[5] K. Hu, D.D. Kulkarni, I. Choi, V.V. Tsukruk, Graphene-polymer nanocomposites for structural and functional applications, Prog. Polym. Sci. 39 (2014) 1934–1972, https://doi.org/10.1016/j.progpolymsci.2014.03.001.
[6] V. Palermo, I.A. Kinloch, S. Ligi, N.M. Pugno, Nanoscale mechanics of graphene and graphene oxide in composites: a scientific and technological perspective, Adv. Mater. 28 (2016) 6232–6238, https://doi.org/10.1002/adma.201505469.
[7] H.D. Wagner, R.A. Vaia, Nanocomposites: issues at the interface, Mater. Today. 7 (2004) 38–42, https://doi.org/10.1016/s1369-7021(04)00507-3.
[8] G. Wang, E. Gao, Z. Dai, L. Liu, Z. Xu, Z. Zhang, Degradation and recovery of graphene/polymer interfaces under cyclic mechanical loading, Compos. Sci. Technol. 149 (2017) 220–227, https://doi.org/10.1016/j.compscitech.2017.06.004.
[9] X. Huang, Z.Y. Yin, S.X. Wu, X.Y. Qi, Q.Y. He, Q.C. Zhang, Q.Y. Yan, F. Boey, H. Zhang, Graphene-based materials: synthesis, characterization, properties, and applications, Small 7 (2011) 1876–1902, https://doi.org/10.1002/smll.201002009.
[10] J.R. Potts, D.R. Dreyer, C.W. Bielawski, R.S. Ruoff, Graphene-based polymer nanocomposites, Polymer 52 (2011) 5–25, https://doi.org/10.1016/j.polymer.2010.11.042.
[11] T. Kuila, S. Bose, A.K. Mishra, P. Khanra, N.H. Kim, J.H. Lee, Chemical functionalization of graphene and its applications, Prog. Mater. Sci. 57 (2012) 1061–1105, https://doi.org/10.1016/j.pmatsci.2012.03.002.
[12] A. Hirsch, J.M. Englert, F. Hauke, Wet chemical functionalization of graphene, Acc. Chem. Res. 46 (2013) 87–96, https://doi.org/10.1021/ar300116q.
[13] J. Shang, Y. Chen, Y. Zhou, L. Liu, G. Wang, X. Li, J. Kuang, Q. Liu, Z. Dai, H. Miao, L. Zhi, Z. Zhang, Effect of folded and crumpled morphologies of graphene oxide platelets on the mechanical performances of polymer nanocomposites, Polymer 68 (2015) 131–139, https://doi.org/10.1016/j.polymer.2015.05.003.
[14] L. Liu, Y. Gao, Q. Liu, J. Kuang, D. Zhou, S. Ju, B. Han, Z. Zhang, High mechanical performance of layered graphene oxide/poly(vinyl alcohol) nanocomposite films, Small 9 (2013) 2466–2472, https://doi.org/10.1002/smll.201300819.
[15] A. Zandiatashbar, G.-H. Lee, S.J. An, S. Lee, N. Mathew, M. Terrones, T. Hayashi, C. R. Picu, J. Hone, N. Koratkar, Effect of defects on the intrinsic strength and stiffness of graphene, Nat. Commun. 5 (2014) 3186, https://doi.org/10.1038/ncomms4186.
[16] L. Liu, J. Zhang, J. Zhao, F. Liu, Mechanical properties of graphene oxides, Nanoscale 4 (2012) 5910–5916, https://doi.org/10.1039/c2nr31164j.
[17] C. Gomez-Navarro, M. Burghard, K. Kern, Elastic properties of chemically derived single graphene sheets, Nano Lett. 8 (2008) 2045–2049, https://doi.org/10.1021/nl801384y.
[18] F. Najafi, G. Wang, T. Cui, A. Anand, S. Mukherjee, T. Filleter, M. Sain, C.V. Singh, Fatigue resistance of atomically thin graphene oxide, Carbon 183 (2021) 780–788, https://doi.org/10.1016/j.carbon.2021.07.062.
[19] F. Najafi, G.R. Wang, S. Mukherjee, T. Cui, T. Filleter, C.V. Singh, Toughening of graphene-based polymer nanocomposites via tuning chemical functionalization, Compos. Sci. Technol. 194 (2020), 108140, https://doi.org/10.1016/j.compscitech.2020.108140.
[20] A. Singh, D. Kumar, Effect of functionalization on the elastic behavior of graphene nanoplatelet-PE nanocomposites with interface consideration using a multiscale approach, Mech. Mater. 132 (2019) 18–30, https://doi.org/10.1016/j.mechmat.2019.02.008.
[21] R.J. Young, L. Gong, I.A. Kinloch, I. Riaz, R. Jalil, K.S. Novoselov, Strain mapping in a graphene monolayer nanocomposite, ACS Nano 5 (2011) 3079–3084, https://doi.org/10.1021/nn2002079.
[22] L. Gong, I.A. Kinloch, R.J. Young, I. Riaz, R. Jalil, K.S. Novoselov, Interfacial stress transfer in a graphene monolayer nanocomposite, Adv. Mater. 22 (2010) 2694–2697, https://doi.org/10.1002/adma.200904264.
[23] T. Jiang, R. Huang, Y. Zhu, Interfacial sliding and buckling of monolayer graphene on a stretchable substrate, Adv. Funct. Mater. 24 (2014) 396–402, https://doi.org/10.1002/adfm.201301999.
[24] M. Liu, Z. Li, X. Zhao, R.J. Young, I.A. Kinloch, Fundamental insights into graphene strain sensing, Nano Lett. 21 (2021) 833–839, https://doi.org/10.1021/acs.nanolett.0c04577.
[25] G. Wang, Z. Dai, L. Liu, H. Hu, Q. Dai, Z. Zhang, Tuning the interfacial mechanical behaviors of monolayer graphene/PMMA nanocomposites, ACS Appl. Mater. Interfaces 8 (2016) 22554–22562, https://doi.org/10.1021/acsami.6b03069.
[26] G.R. Wang, L.Q. Liu, Z.H. Dai, Q. Liu, H. Miao, Z. Zhang, Biaxial compressive behavior of embedded monolayer graphene inside flexible poly (methyl methacrylate) matrix, Carbon 86 (2015) 69–77, https://doi.org/10.1016/j.carbon.2015.01.022.
[27] K.M. Liechti, Characterizing the interfacial behavior of 2D materials: a review, Exp. Mech. 59 (2019) 395–412, https://doi.org/10.1007/s11340-019-00475-6.

[28] Z. Dai, L. Liu, Z. Zhang, Strain engineering of 2D materials: issues and opportunities at the interface, Adv. Mater. 31 (2019), 1805417, https://doi.org/10.1002/adma.201805417.
[29] J.E. Sader, J.W.M. Chon, P. Mulvaney, Calibration of rectangular atomic force microscope cantilevers, Rev. Sci. Instrum. 70 (1999) 3967–3969, https://doi.org/10.1063/1.1150021.
[30] J.R. Vig, UV ozone cleaning of surfaces, J. Vac. Sci. Technol. 3 (1985) 1027–1034, https://doi.org/10.1116/1.573115.
[31] Y. Si, E.T. Samulski, Synthesis of water soluble graphene, Nano Lett. 8 (2008) 1679–1682, https://doi.org/10.1021/nl080604h.
[32] A.C. Ferrari, J.C. Meyer, V. Scardaci, C. Casiraghi, M. Lazzeri, F. Mauri, S. Piscanec, D. Jiang, K.S. Novoselov, S. Roth, A.K. Geim, Raman spectrum of graphene and graphene layers, Phys. Rev. Lett. 97 (2006), 187401, https://doi.org/10.1103/PhysRevLett.97.187401.
[33] K.N. Kudin, B. Ozbas, H.C. Schniepp, R.K. Prud'homme, I.A. Aksay, R. Car, Raman spectra of graphite oxide and functionalized graphene sheets, Nano Lett. 8 (2008) 36–41, https://doi.org/10.1021/nl071822y.
[34] A.J. Pollard, B. Brennan, H. Stec, B.J. Tyler, M.P. Seah, I.S. Gilmore, D. Roy, Quantitative characterization of defect size in graphene using Raman spectroscopy, Appl. Phys. Lett. 105 (2014), 253107, https://doi.org/10.1063/1.4905128.
[35] N. Ferralis, Probing mechanical properties of graphene with Raman spectroscopy, J. Mater. Sci. 45 (2010) 5135–5149, https://doi.org/10.1007/s10853-010-4673-3.
[36] D.G. Papageorgiou, Z. Li, M. Liu, I.A. Kinloch, R.J. Young, Mechanisms of mechanical reinforcement by graphene and carbon nanotubes in polymer nanocomposites, Nanoscale 12 (2020) 2228–2267, https://doi.org/10.1039/c9nr06952f.
[37] W. Qiu, Y.L. Kang, Mechanical behavior study of microdevice and nanomaterials by Raman spectroscopy: a review, Chin. Sci. Bull. 59 (2014) 2811–2824, https://doi.org/10.1007/s11434-014-0401-8.
[38] T.M.G. Mohiuddin, A. Lombardo, R.R. Nair, A. Bonetti, G. Savini, R. Jalil, N. Bonini, D.M. Basko, C. Galiotis, N. Marzari, K.S. Novoselov, A.K. Geim, A. C. Ferrari, Uniaxial strain in graphene by Raman spectroscopy: G peak splitting, gruneisen parameters, and sample orientation, Phys. Rev. B 79 (2009), 205433, https://doi.org/10.1103/PhysRevB.79.205433.
[39] Z. Dai, Y. Hou, D.A. Sanchez, G. Wang, C.J. Brennan, Z. Zhang, L. Liu, N. Lu, Interface-governed deformation of nanobubbles and nanotents formed by two-dimensional materials, Phys. Rev. Lett. 121 (2018) 266101, https://doi.org/10.1103/PhysRevLett.121.266101.
[40] G. Anagnostopoulos, C. Androulidakis, E.N. Koukaras, G. Tsoukleri, I. Polyzos, J. Parthenios, K. Papagelis, C. Galiotis, Stress transfer mechanisms at the submicron level for graphene/polymer systems, ACS Appl. Mater. Interfaces 7 (2015) 4216–4223, https://doi.org/10.1021/am508482n.
[41] Z. Dai, G. Wang, L. Liu, Y. Hou, Y. Wei, Z. Zhang, Mechanical behavior and properties of hydrogen bonded graphene/polymer nano-interfaces, Compos. Sci. Technol. 136 (2016) 1–9, https://doi.org/10.1016/j.compscitech.2016.09.005.
[42] G. Guo, Y. Zhu, Cohesive-shear-lag modeling of interfacial stress transfer between a monolayer graphene and a polymer substrate, J. Appl. Mech. 82 (2015), 031005, https://doi.org/10.1115/1.4029635.
[43] A.K. Geim, K.S. Novoselov, The rise of graphene, Nat. Mater. 6 (2007) 183–191, https://doi.org/10.1038/nmat1849.
[44] Z. Dai, N. Lu, Poking and bulging of suspended thin sheets: slippage, instabilities, and metrology, J. Mech. Phys. Solid. 149 (2021), 104320, https://doi.org/10.1016/j.jmps.2021.104320.
[45] D. Vella, B. Davidovitch, Indentation metrology of clamped, ultra-thin elastic sheets, Soft Matter 13 (2017) 2264–2278, https://doi.org/10.1039/c6sm02451c.
[46] Z. Dai, G. Wang, Z. Zheng, Y. Wang, S. Zhang, X. Qi, P. Tan, L. Liu, Z. Xu, Q. Li, Z. Cheng, Z. Zhang, Mechanical responses of boron-doped monolayer graphene, Carbon 147 (2019) 594–601, https://doi.org/10.1016/j.carbon.2019.03.014.
[47] J.H. Lee, A. Avsar, J. Jung, J.Y. Tan, K. Watanabe, T. Taniguchi, S. Natarajan, G. Eda, S. Adam, A.H.C. Neto, B. Oezyilmaz, Van der Waals force, A dominant factor for reactivity of graphene, Nano Lett. 15 (2015) 319–325, https://doi.org/10.1021/nl5036012.
[48] G. Wang, L. Liu, Z. Zhang, Interface mechanics in carbon nanomaterials-based nanocomposites, Compas.part A. 141 (2021), 106212, https://doi.org/10.1016/j.compositesa.2020.106212.
[49] P. Liu, Z. Jin, G. Katsukis, L.W. Drahushuk, S. Shimizu, C.-J. Shih, E.D. Wetzel, J. K. Taggart-Scarff, B. Qing, K.J. Van Vliet, R. Li, B.L. Wardle, M.S. Strano, Layered and scrolled nanocomposites with aligned semi-infinite graphene inclusions at the platelet limit, Science 353 (2016) 364–367, https://doi.org/10.1126/science.aaf4362.
[50] R.J. Young, M. Liu, I.A. Kinloch, S. Li, X. Zhao, C. Valles, D.G. Papageorgiou, The mechanics of reinforcement of polymers by graphene nanoplatelets, Compos. Sci. Technol. 154 (2018) 110–116, https://doi.org/10.1016/j.compscitech.2017.11.007.